Relationship between activity and stability: Design and characterization of stable variants of human frataxin

Ignacio Hugo Castro, Mauro Bringas, Davide Doni, Martin Ezequiel Noguera, Luciana Capece, Martín Aran, Matías Blaustein, Paola Costantini, Javier Santos

PII: S0003-9861(20)30500-2

DOI: https://doi.org/10.1016/j.abb.2020.108491

Reference: YABBI 108491

To appear in: *Archives of Biochemistry and Biophysics*

Received Date: 5 May 2020

Revised Date: 26 June 2020

Accepted Date: 8 July 2020

Please cite this article as: I.H. Castro, M. Bringas, D. Doni, M.E. Noguera, L. Capece, Martí. Aran, Matí. Blaustein, P. Costantini, J. Santos, Relationship between activity and stability: Design and characterization of stable variants of human frataxin, *Archives of Biochemistry and Biophysics* (2020), doi: https://doi.org/10.1016/j.abb.2020.108491.

Relationship Between Activity and Stability: Design and Characterization of Stable Variants of Human Frataxin

Ignacio Hugo Castro,[1] Mauro Bringas,[2] Davide Doni,[3] Martin Ezequiel Noguera,[1,4] Luciana Capece,[2] Martín Aran,[5] Matías Blaustein,[1,6] Paola Costantini,[3] and Javier Santos[1, 6,7,*]

[1]Instituto de Biociencias, Biotecnología y Biología Traslacional (iB[3]). Departamento de Fisiología y Biología Molecular y Celular, Facultad de Ciencias Exactas y Naturales, Universidad de Buenos Aires. Intendente Güiraldes 2160, Ciudad Universitaria, C1428EGA, Buenos Aires, Argentina.
[2]Departamento de Química Inorgánica, Analítica y Química Física, Facultad de Ciencias Exactas y Naturales, Universidad de Buenos Aires. Instituto de Química Física de los Materiales, Medio Ambiente y Energía (INQUIMAE CONICET), C1428EGA, Buenos Aires, Argentina.
[3]Department of Biology, University of Padova, Viale G. Colombo 3, 35131 Padova, Italy.
[4]Instituto de Química y Fisicoquímica Biológicas, Dr. Alejandro Paladini, Universidad de Buenos Aires, CONICET, Junín 956, C1113AAD, Buenos Aires, Argentina.
[5]Fundación Instituto Leloir, IIBBA-CONICET, and Plataforma Argentina de Biología Estructural y Metabolómica PLABEM, Av. Patricias Argentinas 435, C1405BWE, Buenos Aires, Argentina.
[6]Consejo Nacional de Investigaciones Científicas y Técnicas. Rivadavia 1917. C1033AAJ. Buenos Aires, Argentina.
[7]Departamento de Química Biológica, Facultad de Ciencias Exactas y Naturales, Universidad de Buenos Aires. Intendente Güiraldes 2160, Ciudad Universitaria, C1428EGA, Buenos Aires, Argentina.

***Corresponding Author:** Javier Santos at javiersantosw@gmail.com

Running Title: Stable variants of Human Frataxin

Keywords: conformational stability, protein-protein interaction, iron-sulfur cluster assembly, frataxin.

Abbreviations: ACP, acyl carrier protein; CD, circular dichroism; CTR, C-terminal region; DLS, dynamic light scattering; Fe-S, iron-sulfur; FRDA, Friedreich's Ataxia; FXN, frataxin; HPLC, high-performance liquid chromatography; ISCU, iron-sulfur cluster assembly enzyme; ISD11, NFS1 interacting protein; NFS1, mitochondrial cysteine desulfurase enzyme; NMR, nuclear magnetic resonance; PAGE, polyacrylamide gel electrophoresis; PDB, Protein Data Bank; SDS, sodium dodecyl sulfate; SEC, size exclusion chromatography.

Highlights:

- A set of frataxin variants spanning a broad range of conformational stabilities was prepared.
- Variants S160I, S160M and A204R were more stable than the wild-type and equally active.
- As in the case of FRDA variant N146K, variant S157I showed higher stability but lower function.
- The triple mutant S160I/L203C/A204R was 2.4 kcal mol^{-1} more stable and resistant to proteolysis, and it was as active as the wild-type variant.
- Internal motions were investigated by molecular dynamics simulations and NMR.
- The study of frataxin variants uncovered the tradeoff between frataxin stability and the cysteine desulfurase supercomplex function.

Abstract

The relationships between conformational dynamics, stability and protein function are not obvious. Frataxin (FXN) is an essential protein that forms part of a supercomplex dedicated to the iron-sulfur (Fe-S) cluster assembly within the mitochondrial matrix. In humans, the loss of FXN expression or a decrease in its functionality results in Friedreich's Ataxia, a cardio-neurodegenerative disease. Recently, the way in which FXN interacts with the rest of the subunits of the supercomplex was uncovered. This opens a window to explore relationships between structural dynamics and function. In this study, we prepared a set of FXN variants spanning a broad range of conformational stabilities. Variants S160I, S160M and A204R were more stable than the wild-type and showed similar biological activity. Additionally, we prepared SILCAR, a variant that combines S160I, L203C and A204R mutations. SILCAR was 2.4 kcal mol^{-1} more stable and equally active. Some of the variants were significantly more resistant to proteolysis than the wild-type FXN. SILCAR showed the highest resistance, suggesting a more rigid structure. It was corroborated by means of molecular dynamics simulations. Relaxation dispersion NMR experiments comparing SILCAR and wild-type variants suggested similar internal motions in the microsecond to millisecond timescale. Instead, variant S157I showed higher denaturation resistance but a significant lower function, similarly to that observed for the FRDA variant N146K. We concluded that the contribution of particular side chains to the conformational stability of FXN might be highly subordinated to their impact on both the protein function and the stability of the functional supercomplex.

Introduction

The relationships between conformational stability, internal motions and protein function are not trivial and are the essence of the protein nature. The alteration of the conformational stability of proteins is a key factor for the development of pathogenicity in several human diseases.

Numerous proteins exert their function by establishing specific protein-protein interactions. Although in some cases they interact transiently, in other cases they form stable protein complexes. The latter is the case of frataxin (FXN), an essential mitochondrial protein of 120 residues, which is nuclearly encoded. FXN is one of several proteins that forms a supercomplex dedicated to the iron-sulfur (Fe-S) cluster assembly within the mitochondrial matrix. A myriad of enzymatic processes depends on its activity. In this supercomplex, FXN works as an activator that simultaneously interacts at least with two different proteins: ISCU, the scaffold protein, and the cysteine desulfurase NFS1, a PLP dependent enzyme that transfers -SH groups from the substrate (cysteine) to ISCU (Fox et al. 2019). It is worthy of note that FXN simultaneously interacts with both NFS1 subunits of the supercomplex (PDB ID: 6NZU).

Remarkably, in humans, the loss of FXN expression or a decrease in its functionality, and the subsequent deficiency in the iron-sulfur cluster (Fe-S) assembly in the mitochondria, result in Friedreich's Ataxia (FRDA), a cardio-neurodegenerative disease (Campuzano et al. 1996; Lamont et al. 1997; Ohshima et al. 1998; Marmolino and Acquaviva 2009; Punga and Buhler 2010; Lufino et al. 2013; Li et al. 2015; Silva et al. 2015; Galea et al. 2016).

Although 95% of FRDA patients exhibit in each allele GAA triplet-repeat expansion in the first intron of the FXN gene, which determines a low expression of

FXN, the remaining 5% of patients have a missense mutation in one of the alleles (in compound heterozygosis with the GAA triplet-repeat expansion in the other allele), modifying the conformational stability and/or the protein function; currently, there is only one report of patients showing homozygous missense mutation, R165C, (Candayan et al. 2019).

Among many other compound variants, G130V (Correia et al. 2008), G137V (Faggianelli et al. 2015), L198R (Faraj et al. 2014), and the truncated form FXN81-193 (ΔCTR) (Roman et al. 2012; Sacca et al. 2013) showed a significant decrease of the conformational stability of the protein. In principle, this feature is expected to yield a concomitant low protein concentration in the cell because of protein degradation. In the case of mutant G137V, no impairment of the structure or activity of the protein was found *in vitro* (Faggianelli et al. 2015); however, low FXN concentration was observed in the patient.

On the other hand, a significant reduction of conformational stability may additionally result in a decrease in protein function as a consequence of the loss of cooperativity with an increase of local unfolding events, the alteration of the internal motions as in the case of L198R or FXN81-193 (ΔCTR) (Faraj et al. 2014).

Some FXN mutations perturb the supercomplex assembly, yielding a decrease in function, without necessarily causing a reduction of the conformational stability of FXN. This is the case of mutations N146K and W155R. The former significantly stabilizes the native conformation of FXN (Bellanda et al. 2019); however, the activity of this variant decreases because N146 is very close to the ISCU-FXN interaction region, adjacent to W155, another key residue that is fundamental for this interaction (Bridwell-Rabb et al. 2011; Schmucker et al. 2011). Thus, the interaction surfaces of ISCU and FXN have coevolved and the contribution to the stability of the residues

involved in coevolution might be highly subordinated to their impact on both protein function and the stability of the functional supercomplex.

Additionally, in principle, FXN interacts with iron by means of its “acidic ridge”, a region of the protein that is very rich in Glu and Asp residues (Huang et al. 2008; Vazquez et al. 2015; Adinolfi et al. 2002; Correia et al. 2008). This metal ion binding process is thought to be relevant for the activation of the supercomplex, and the influence of these acidic residues on conformational stability was previously studied by the group of Gomes (Correia et al. 2010). The mutation of the acidic residues to alanine resulted in a substantial stabilization of the native conformation. It is worthy of mention that several acidic residues are also involved in the interaction between FXN and NFS1 (Schmucker et al. 2011; Fox et al. 2019).

The behavior of the alanine variants of the acidic ridge added to that of the N146K mutant suggest a substantial tradeoff between conformational stability and function. On the other hand, the L203C variant (Faraj et al. 2016; Faraj et al. 2019), in which a core leucine residue is replaced by a cysteine, is more stable than the wild-type FXN and exhibited similar cysteine desulfurase activation. Then, a more complex relationship between stability and function needs to be invoked to explain these observations.

In this context, we decided to look for other FXN variants more stable than the wild-type protein and, at least, equally active *in vitro* and *in vivo*. Taking this into account, we explored the FXN structure by means of bioinformatic tools in order to locate residues that might be replaced by another one, increasing thermodynamic stability. We found a series of feasible mutants. They were prepared and studied *in vitro*. Conformational features and stability and the capability of activating the supercomplex were analyzed side by side.

Materials and Methods

Bioinformatics

Stability and mutational effect calculations were performed using FOLDX (Schymkowitz et al. 2005). For these calculations, PDB ID: 1EKG (Dhe-Paganon et al. 2000) was analyzed. Briefly, first all positions were evaluated by means of FOLDX to find positions that might be mutated producing an increase in the conformational stability of the protein. The PositionScan was applied using repair tool. It mutates each amino acid to the other 19.

Mutagenesis, Protein Expression and Purification

Mutagenesis was carried out using the Q5® Site-Directed Mutagenesis Kit (New England Biolabs, U.S.A.). Wild-type FXN (residues 90-210) and mutants were expressed and purified as previously described for the wild-type variant (Faraj et al. 2014). Purity was > 98 % as evaluated in SDS-PAGE. Identity was verified by DNA sequencing using Macrogen facility and by mass spectrometry analysis. The latter was performed in the National Laboratory of Research and Services in Peptides and Proteins using an LCQ DUO ESI ion trap (Thermo Finnigan) or QExactive Orbitrap (Thermo Scientific) spectrometers.

For ^{15}N-labeled protein, production cultures were grown in M9 minimal medium supplemented with ^{15}N-NH_4Cl obtained from Cambridge Isotope Laboratories (Andover, MA) and purified as the unlabeled samples. Extinction coefficients were calculated from amino acid sequences using the ProtParam tool on the ExPASy Server (Wilkins et al. 1999).

The DNA sequence corresponding to ISCU2 was optimized for *E. coli* expression by Explora Biotech (Rome Italy) and cloned in a pE22b vector, with a C-

terminal His6 tag. Protein was induced by the addition of 1mM IPTG (3h, 37°C and 250 rpm). The protein was purified using a Ni^{2+}-NTA-agarose column equilibrated in a buffer 20 mM Tris-HCl, 300 mM NaCl, pH 7.5. The elution was performed with a buffer 20 mM Tris-HCl, 300 mM NaCl, 500 mM imidazole, pH 7.5.

The DNA sequences corresponding to the human NFS1, ISD11 and ACP proteins where optimized for *E. coli* expression by Bio Basic (Markham ON, Canada). The cysteine desulfurase variant NFS1Δ55 (mature form, with an N-terminal His6 tag) and the ISD11 sequences were cloned in a pETduet plasmid and ACP was cloned in a pACYCDuet-1 vector. To prepare the protein complex $(NFS1/ACP\text{-}ISD11)_2$, the three proteins NFS1, ISD11 and ACP proteins were induced by the addition of 1mM IPTG and co-expressed (overnight, 20 °C and 250 rpm). Purification was carried out using a Ni^{2+}-NTA-agarose column equilibrated in a buffer 20 mM Tris-HCl, 300 mM NaCl, 20 mM imidazole, pH 8.0. The elution was performed with a buffer 20 mM Tris-HCl, 300 mM NaCl, 500 mM imidazole, pH 8.0.

Circular Dichroism Spectroscopy

Circular dichroism (CD) measurements were carried out in a Jasco J-815 spectropolarimeter. Near-UV CD spectra were collected using a 1.0 path length cell, thermostatized at 20 °C. Protein concentration was 25 μM and the buffer was 20 mM Tris-HCl, 100 mM NaCl, pH 7.0. Data were acquired at a scan speed of 20 nm min^{-1}, with a 1-nm bandwidth and a 0.1-nm data-pitch. Five scans for each sample were averaged, and the blank spectrum was subtracted to the average.

Light Scattering and the Hydrodynamic Behavior of the FXN Mutants

The hydrodynamic radius (R_h) of the FXN mutants was investigated using Dynamic Light Scattering (DLS, Zetaziser Nano-S, Malvern). Protein concentration was in the range of 70-140 μM (1-2 mg mL^{-1}). The buffer was 20 mM Tris-HCl, 100 mM NaCl, pH 7.0. The experiments were carried out at 25 °C. On average, 10 runs were performed. Size distributions weighted by particle number were obtained.

Additionally, SEC-HPLC was performed using a Superose-6 column (GE Healthcare). Protein concentration was 25-75 μM, a volume of 50μL was typically injected, and running buffer was 20 mM Tris-HCl, 100 mM NaCl, 1 mM EDTA, at pH 7.0. The experiment was carried out at room temperature (~25 °C) at a 0.5 mL/min flow rate. A JASCO HPLC instrument was used. It was equipped with an automatic injector, a quaternary pump and a UV-VIS UV-2075 (elution was monitored at 280 nm).

Thermal Shift Assay

Temperature-induced denaturation of FXN variants was monitored by the change in the Sypro Orange dye fluorescence using protein at a 5.0 μM concentration in 50 mM sodium phosphate buffer, pH 7.0. Samples without protein were also included as controls. The dye was used at 2 × (as suggested by Thermo Fisher Scientific). The temperature slope was 1 °C min^{-1} (from 20 to 90 °C). Excitation and emission ranges were 470–500 and 540–700 nm, respectively. The fluorescence signal was quenched in the aqueous environment but became unquenched when the probe bound to the apolar residues upon unfolding. Experiments by triplicate were carried out in a Step One Real-Time-PCR instrument (Applied Biosystems, CA, U.S.A.).

Equilibrium Unfolding Experiments

Isothermal unfolding experiments were performed incubating each FXN variant (3.7 μM) with different concentrations of denaturant (urea) in a buffer solution of 20 mM Tris-HCl, 100 mM NaCl, 1 mM EDTA, at pH 7.0 for 5 h at room temperature. A fresh urea solution (approximately 9.2 M) was prepared for each experiment, and the exact urea concentration was determined using refractive index measurements, using a Palm Abbe digital refractometer (Misco). Tryptophan fluorescence spectra measurements were taken at 20° C. Excitation was carried out at 295 nm and spectra were acquired between 305 and 500 nm.

To calculate thermodynamic parameters, a linear dependence of the standard free energy of unfolding (ΔG°_{NU}) on denaturant concentration was assumed:

$$\Delta G^{0}_{\mathrm{NU}} = \Delta G^{0}_{\mathrm{NU,H2O}} - m_{\mathrm{NU}}[urea] \quad (1)$$

where $\Delta G^{\circ}_{\mathrm{NU,\ H20}}$ is the free energy of unfolding in the absence of denaturant and m_{NU} is the dependence of free energy on denaturant. Defining C_{m} as the denaturant concentration in which $\Delta G^{\circ}_{\mathrm{NU}} = 0$, it is deduced that:

$$\Delta G^{0}_{\mathrm{NU}} = m_{\mathrm{NU}}(C_{\mathrm{m}} - [urea]) \quad (2)$$

A two–state unfolding mechanism was assumed, and the following equation was fitted to data:

$$S = \frac{\left(S_{0,\mathrm{N}} + m_{\mathrm{N}}[urea]\right) + \left(S_{0,\mathrm{U}} + m_{\mathrm{U}}[urea]\right)e^{\left(\frac{m_{NU}[urea] - C_{\mathrm{m}}}{RT}\right)}}{1 + e^{\left(\frac{m_{\mathrm{NU}}[urea] - C_{\mathrm{m}}}{RT}\right)}} \quad (3)$$

where $S_{0,\mathrm{N}}$ and $S_{0,\mathrm{U}}$ are the intrinsic CD signals for the native and unfolded states, respectively. Parameters m_{N} and m_{U} are the slopes of the pre- and post-transitions, respectively, assuming the linear dependences of $S_{0,\mathrm{N}}$ and $S_{0,\mathrm{U}}$ signals with urea concentration.

The correlation obtained in this work between the observed T_m values (unfolding monitored by Sypro-orange florescence) and free energy differences (urea unfolding experiments monitored by Trp fluorescence) was $y = (0.25 \pm 0.01)\ x - (16.27 \pm 0.54)$, with an $R^2 = 0.99$.

Controlled Proteolysis

Resistance to proteolysis of the FXN variants was analyzed by SDS-PAGE and RP-HPLC profiles (C18). The variants at 1 mg mL^{-1} protein concentration were incubated during 5h reactions at 40 °C in buffer 20 mM Tris-HCl, 100mM NaCl, 1mM EDTA, pH 7.0 in the presence or in the absence of chymotrypsin (1:100 protease: protein ratio). The reactions were stopped by the addition of 2 × sample buffer for SDS-PAGE analysis and 1mM PMSF (final concentration), or 1mM PMSF (final concentration) and 0.05% (*v/v*) TFA for RP-HPLC. Protein controls without protease were simultaneously incubated, for the same period of time, and under exactly the same conditions of buffer and temperature. PMSF was added after the incubation. For HPLC, a JASCO system, equipped with an autoinjector, an oven (thermostatized at 25 °C) an and UV detector, was used. A gradient from 0 to 100% acetonitrile was performed (0.05% TFA (*v/v*) was added to the solvents). The column used was an analytical C18 (Higgins Analytical, Inc. U.S.A.) and flow was 1.0 mL min^{-1} Peptides were monitored at 220 nm. Wild-type FXN was included as a reference.

NFS1 Cysteine Desulfurase Activity

Enzymatic desulfurization of cysteine to alanine and sulfide by the NFS1/ACP-ISD11/ISCU/FXN supercomplex was determined by the methylene blue method. Concentrations of proteins, substrate and the reducing agent DTT were set according to

a previous paper by Tsai and Barondeau (Tsai and Barondeau 2010). Reactions contained 1.0 μM NFS1, 1.0 μM ACP-ISD11, 3.0 μM ISCU and 3.0 μM FXN, and samples were supplemented with 10 μM PLP, 2 mM DTT, and 1.0 μM $FeSO_4$ (final concentrations). The reaction buffer was 50 mM Tris-HCl and 200 mM NaCl, pH 8.0, and reactions were started by the addition of 1 mM cysteine. Samples were incubated at room temperature for 30 min. H_2S production was stopped by the addition of 50 μL of 20 mM N,N-dimethyl p-phenylenediamine in 7.2 M HCl and 50 μL of 30 mM $FeCl_3$ (prepared in 1.2 M HCl). Under these conditions, the production of methylene blue took 20 min. After that, samples were centrifuged for 5 min at 12000*g*, and the supernatant was separated. Absorbance at 670 nm was measured.

NMR Samples, Data Acquisition and Processing

Samples for NMR experiments contained 0.45 mM ^{15}N-labelled protein in 20 mM Tris-HCl, 100 mM NaCl, 1.0 mM EDTA, at pH 7.0, supplemented with 5% D_2O. NMR experiments were performed at 22° C in a Bruker 600 MHz Avance III spectrometer equipped with a TXI probe. The NMR data were processed with NMRPipe (Delaglio et al. 1995) and analyzed using NMRViewJ (Johnson 2004).

Backbone Amide Resonance Assignment

The chemical shift assignments of nitrogen, and amide and alpha protons of loop-1 variants were performed by 3D ^{15}N-NOESY-HSQC and ^{15}N-TOCSY-HSQC experiments (100 and 30 ms of mixing times, respectively), based on the available chemical shifts of the full-length C-terminal domain of FXN (BMRB 4342) (Musco et al. 1999). The ^{1}H-^{15}N-NOESY-HSQC spectrum of the wild-type FXN was recorded to assist in the assignment.

Relaxation Dispersion Experiments

Carr-Purcell Meiboom-Gill relaxation dispersion experiments were performed using published methods (Palmer et al. 2001; Farber and Mittermaier 2015). In these experiments, variable trains of refocusing pulses were applied during a constant relaxation period to suppress spectral broadening due to conformational exchange (Palmer et al. 2001). A constant-time relaxation-compensated pulse program was used for all variants, setting the constant time period (T_{CPMG}) to 100 ms in combination with the following CPMG frequencies (ν_{CPMG}): 40, 80, 120, 160, 200, 240, 280, 320, 360, 400, 480, 520, 600, 680, 760, 840, 920, 1000, 1080 and 1200 Hz. Two-dimensional data sets were acquired in an interleaved manner, with an interscan delay of 3 s and 256 increments in the nitrogen dimension. The observed transverse relaxation rate (R_2^{Obs}) for each frequency point was obtained from the signal intensity measured at the end of the T_{CPMG} period according to:

$$R_2^{Obs}(\nu_{\mathrm{CPMG}}) = \frac{-1}{T_{\mathrm{CPMG}}} ln\left(\frac{I(\nu_{\mathrm{CPMG}})}{I_0}\right) \quad (4)$$

where $I(\nu_{\mathrm{CPMG}})$ and I_0 are the intensities of a given cross-peak measured with or without the CPMG period, respectively, for a specific spin-lock frequency (ν_{CPMG}).

The contribution of the exchange to the signal relaxation rate (R_{ex}) is estimated by:

$$R_2^{\mathrm{Obs}}(\nu_{\mathrm{CPMG}} \to 0) = R_{\mathrm{ex}} + R_2^{\mathrm{Obs}}(\nu_{\mathrm{CPMG}} \to \infty) \quad (5)$$

where $R_2^{\mathrm{Obs}}(\nu_{\mathrm{CPMG}} \to \infty)$ is the intrinsic relaxation rate in the absence of exchange, at infinite ν_{CPMG}, estimated from the average of the R_2^{Obs} at the 3 highest ν_{CPMG}, whereas $R_2^{\mathrm{Obs}}(\nu_{\mathrm{CPMG}} \to 0)$ was approximated as R_2^{Obs} at the lowest ν_{CPMG}. The experiment was carried out at two different magnetic field strengths (14.1 and 16.5 T) and dispersion profiles were then analyzed as in a previous work (Noguera et al. 2017). Dispersion

profiles were then analyzed using the Sherekhan server (Mazur et al. 2013) to fit a completely general two-site exchange model to the dispersion data acquired at both magnetic fields, using the following equations:

$$R_2^{\text{obs}}\left(1/\tau_{CP}\right) =$$

$$\frac{1}{2}\left(R_{2\,\text{A}}^{o} + R_{2\,\text{B}}^{o} + k_{\text{ex}} - \frac{1}{\tau_{CP}}\cosh^{-1}[D_+ \cosh(\eta_+) - D_- \cos(\eta_-)]\right) \quad (6)$$

in which, k_{ex} is the observed constant for the conformational exchange, τ_{CP} is the delay between 180° pulses in the CPMG pulse train, $R_{2\text{A}}^{o}$ and $R_{2\,\text{B}}^{o}$ are the intrinsic (exchange-free and independent of the ν_{CPMG}) transverse relaxation rate constants for states A and B, respectively (it is assumed that $R_{2\,\text{A}}^{o} = R_{2\,\text{B}}^{o}$) and,

$$D_{\pm} = \frac{1}{2}\left[\pm 1 + \frac{\psi + 2\Delta\omega^2}{(\psi^2+\zeta^2)^{1/2}}\right] \quad (7)$$

$$\eta_{\pm} = \frac{\tau_{CP}}{\sqrt{2}}\left[\pm\psi + (\psi^2 + \zeta^2)^{1/2}\right]^{1/2} \quad (8)$$

$$\psi = \left(R_{2\,\text{A}}^{o} - R_{2\,\text{B}}^{o} - p_A k_{\text{ex}} + p_B k_{\text{ex}}\right)^2 - \Delta\omega^2 + 4\,p_A p_B k_{ex}^2 \quad (9)$$

$$\zeta = 2\Delta\omega\left(R_{2\,\text{A}}^{o} - R_{2\,\text{B}}^{o} - p_A k_{\text{ex}} + p_B k_{\text{ex}}\right) \quad (10)$$

where $\Delta\omega$ is the chemical shift difference between states A and B, p_{A} and p_{B} are the populations of the states A and B. Finally, a F-test was carried out to confirm that the identified residues behave as a cluster.

The R_2^{obs} profile corresponding to each residue was individually fitted using the NESSY program (Bieri and Gooley 2011). The relaxation profile was better described by an exchanging model compared with the no-exchange model, according to the corrected Akaike Information Criterion. This preliminary analysis was performed separately for the two protein variants and the two static magnetic fields. Most of the significant exchanging residues in the SILCAR variant are the same than the ones previously identified for the wild-type variant in our previous studies (Noguera et al.

2017). On the other hand, we were unable to assign the L103 residue in SILCAR and some relaxation profiles were too noisy precluding a confident estimation of the exchanging parameter, so these later profiles were excluded from the global fit. As a result, eight residues were included in a global fit using a general two-state equation for chemical exchange.

Molecular Dynamics Simulations

The coordinates corresponding to human FXN (PDB ID: 1EKG) and the SILCAR model obtained by *in silico* mutation of the wild-type structure using FOLDX were solvated with the TIP3P water model molecules (Jorgensen et al. 2015). Protonation states of amino acid residues were set to correspond to those at pH 7.0. As in previous works, in the case of His residues, δ or ε protonation was established to favor hydrogen bond formation (Capece et al. 2006). A standard minimization protocol was applied to the resulting structures to specifically remove steric clashes. The systems were heated up from 100 to the desired temperatures (300 or 340K) using the Berendsen thermostat and constant volume conditions. 800 ps isobaric molecular dynamics were run to achieve an appropriate density. A 2-fs time step was used, and the SHAKE algorithm was applied (Ryckaert et al. 1977). Unrestrained 400 ns production MD simulations were performed with Amber 18 (Case et al. 2018), using the ff14SB force field (Maier et al. 2015). Analysis of production runs were performed using CPPTRAJ software from AmberTools. The fraction of time in which H-bond interaction is formed was calculated by integrating the first peak (from 3 to approximately 4.5 Å) of the probability density function.

Results

Finding Point Mutants More Stable than the Wild-Type FXN

To evaluate the contribution of each amino acid residue to conformational stability, the FXN structure (PDB ID: 1EKG) was examined by means of the FOLDX bioinformatic tool (**Figure 1**). A list of approximately 220 potential variants was found, in which the predicted stability was at least 0.5 kcal mol^{-1} higher than that of the wild-type FXN. Next, these mutants were analyzed by considering the structure of the supercomplex $[NFS1/ACP\text{-}ISD11/ISCU/FXN]_2$ (PDB ID: 6NZU). Our purpose was to avoid mutations of positions involved in protein-protein interactions. Potential mutations of residues involved in FRDA sites or in the immediate vicinity of these residues were also discarded. However, the exception was K147M, near N146, a position involved in FRDA (N146K variant). K147M was not discarded given the possibility of blocking the ubiquitination site K147 in order to alter degradation *in vivo* (Benini et al. 2017; Rufini et al. 2011). Additionally, we discarded mutations of those residues located in the iron binding region (helix α1, loop-1 and strand β1), given the eventual disruption of metal-FXN and cysteine desulfurase NFS1-FXN interactions.

This protocol constrained the set of variants to a reduced group of approximately twenty plausible positions. In this context, we decided to prepare and study a preliminary set of seven mutants: K147M, S157I, S160I, S160M, A193L, T196I and A204R. We included mutant A204M in order to investigate the effect of a long side chain at this position, compared to the electrostatic effect of the long and positively charged side chain as the one corresponding to the arginine residue (**Table 1**), and we also studied the L203C variant previously identified by our laboratory as a stabilizing mutation ($\Delta\Delta G^{o}_{NU}$= 1.0 kcal mol^{-1}). Remarkably, the prediction of the effect of the

cysteine sidechain is not captured by FOLDX at all; instead, it is predicted as a highly destabilizing mutation (**Figure 1,** expected $\Delta\Delta G^{o}_{NU}$= -3.0 kcal mol^{-1}).

The conformational stability of the variants was also inferred from the FXN protein structure using the Dynamut tool (Rodrigues et al. 2018), which included dynamic information for the predictions (**Table 1**). Whereas FOLDX predicted K147M significantly more stable than the wild-type, Dynamut predicted this mutation may be only slightly stabilizing; the same occurred for mutation T196I. On the other hand, A204M, which was predicted as a stabilizing mutation by FOLDX, was predicted as destabilizing by Dynamut. In addition, Dynamut failed to predict the stabilizing effect of L203C.

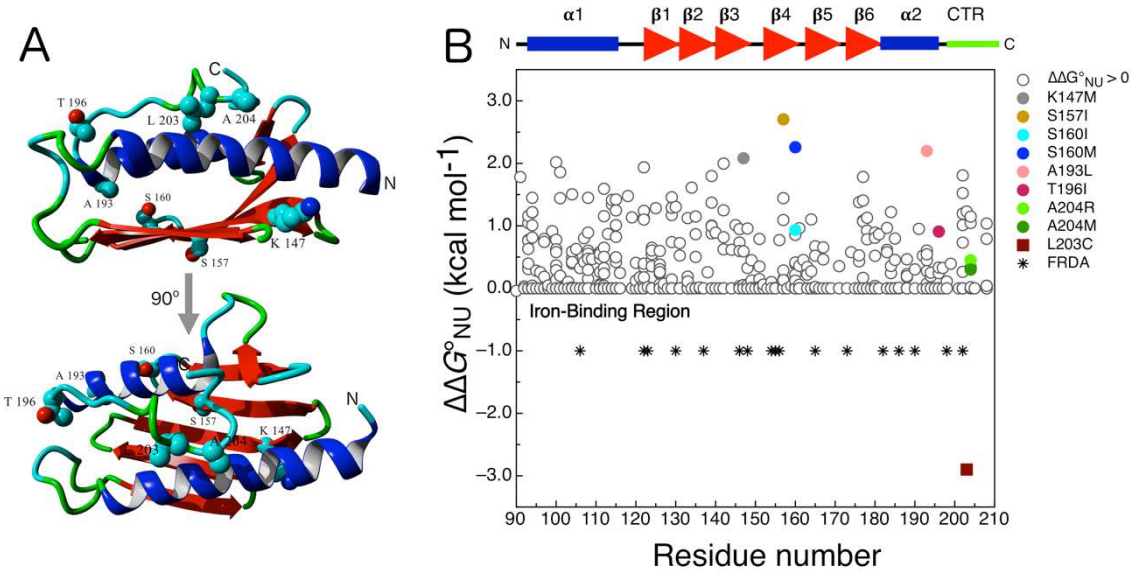

Figure 1. Bioinformatic Inspection of FXN by FOLDX. (A) Ribbon representation of FXN structure showing the residues mutated in this work. Protein representations were prepared using YASARA (Krieger and Vriend 2014). (B) The structure (residues 90 to 108) was analyzed using FOLDX (Schymkowitz et al. 2005) and mutations that exhibited $\Delta\Delta G^{o}_{NU} > 0$ were plotted (empty circles). Mutations prepared in this work are highlighted with color circles. The $\Delta\Delta G^{o}_{NU}$ prediction for L203C mutant is shown by a full-brown-square. $\Delta\Delta G^{o}_{NU} = \Delta G^{o}_{NU\ mutant\ FXN} - \Delta G^{o}_{NU\ wild-type\ FXN}$ (positive values correspond to stabilizing mutations, e.g., L203C is predicted as destabilizing mutation). FRDA mutants currently known are indicated by asterisks at positions 106, 122, 123, 130, 137, 146, 148, 154, 155, 156, 165, 173, 182, 186, 190, 198 and 202. Note that the asterisks are not associated to $\Delta\Delta G^{o}_{NU}$values; they are only included to indicate the

residue involved. Secondary structure elements are depicted at the top of panel B; CTR is the C-terminal region.

The FRDA variants D122Y, G130V, W155R and L198R that were previously shown to be less stable than wild-type FXN ($\Delta\Delta G°_{NU}$= -2.1, -2.9, -1.4 and -4.2 kcal mol^{-1}, respectively, (Correia et al. 2008; Faraj et al. 2016)) were included as a reference in our analysis. Additionally, the FRDA mutant N146K, which exhibits a higher resistance to thermal denaturation than wild-type FXN (observed ΔT_m ~ 5 °C), was also integrated to the set of proteins analyzed (Bellanda et al. 2019).

The set of point mutant variants was prepared as described in Materials and Methods, purified (>98%, SDS-PAGE and HPLC, data not shown) and studied. All variants were soluble. The analysis of dynamic light scattering experiments along with size exclusion chromatography (SEC-HPLC) showed that all of the variants are folded and behave as compact monomers in solution (**Figure 2A**, and **Table 1**). The observed molecular mass values fall in the range 15000-13600 Da, as inferred by means of the calibration curve (**Figure 2A, inset**).

We analyzed the tertiary structure of the variants by circular dichroism (CD) spectroscopy in the near-UV region. All the variants showed near-UV CD spectra compatible with a fully conserved structure (**Figure 2**); similar band shapes and intensities were observed. This result indicated comparable asymmetric environments for the aromatic residues, among the FXN variants.

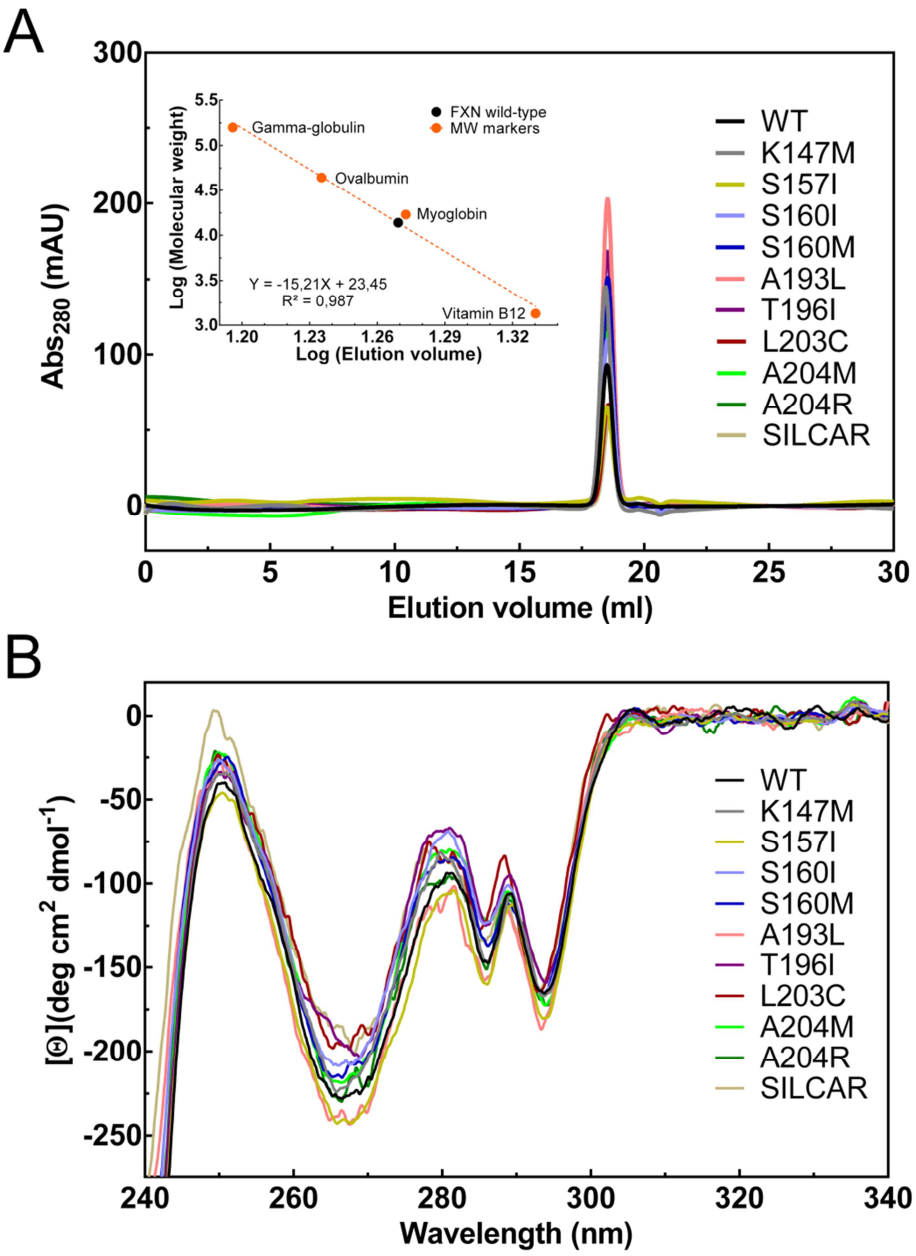

Figure 2. Characterization of the FXN Variants. (A) Characterization of the hydrodynamic behavior of the FXN variants by SEC-HPLC. Protein concentration was 25 to 75 µM. Buffer was 20 mM Tris-HCl, 100 mM NaCl, pH 7.0. The inset shows the correlation between molecular weight and elution volume obtained from a chromatogram corresponding to the molecular weight markers gammaglobulin (158kDa), ovoalbumin (44kDa), myoglobin (17kDa), and vitamin B12 (1350Da). (B) Characterization of the tertiary structure of the FXN variants by near-UV CD spectroscopy. Protein concentration was 25 µM and the buffer was 20 mM Tris-HCl, 100 mM NaCl, pH 7.0. Spectra were collected at 20 °C.

Conformational Stability of Point Mutants

Next, the resistance to temperature-induced unfolding followed by Sypro-orange fluorescence was explored (**Figure 3**). Five of the seven mutants showed the observed T_m higher than the wild-type variant (observed ΔT_m > 2°C), whereas K147M and A204M mutants displayed considerably lower observed T_m values (observed ΔT_m < 2°C), suggesting that conformational stability of the latter variants might be lower than that of the wild-type FXN. Therefore, (i) a long side chain at position 204 is not enough to yield FXN stabilization; (ii) K147M, which was predicted as a stabilizing mutation, on the contrary, is slightly destabilizing.

FRDA variants prepared as controls D122Y, G130V, W155R and L198R exhibited considerably lower observed T_m value than the wild-type protein, compatible with a destabilization of FXN conformation, whereas N146K showed a marked increase in the observed T_m, compatible with the stabilization of the native state of FXN.

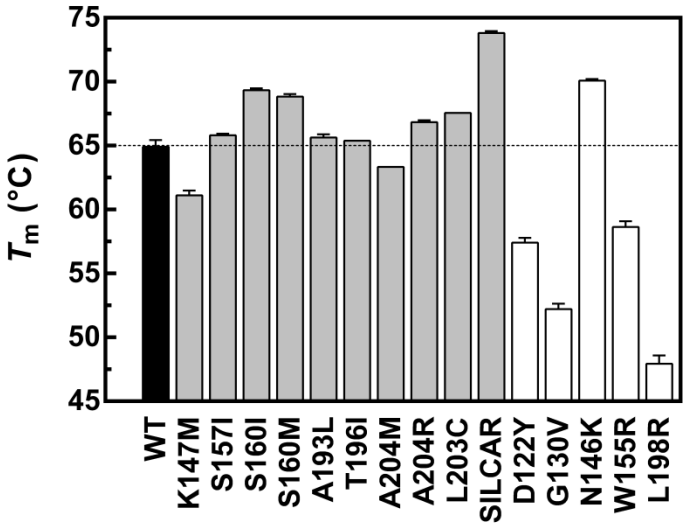

Figure 3. Temperature-Induced Unfolding Followed by Sypro-Orange Fluorescence. Protein was at 5.0 μM. Buffer was 50 mM sodium phosphate, pH 7.0. The temperature slope was 1 °C min^{-1} (from 20 to 90 °C). Excitation and emission

ranges were 470–500 and 540–700 nm, respectively. Grey bars correspond to the designed variants, whereas white bars correspond to FRDA FXN variants.

Remarkably, three variants (S160I, S160M and A204R) exhibited substantially higher observed T_m values than the rest of the variants (**Table 2**), suggesting that these mutations might have stabilizing effects. In particular, S160I and S160M exhibited observed T_m values even higher that the stable variant L203C.

To evaluate more exhaustively the effect of the mutations on conformational stability, we carried out isothermal urea-induced unfolding experiments followed by tryptophan fluorescence for S160I, S160M, A204R. Wild-type and L203C variants were studied side by side with the mutants.

Human FXN has three tryptophan residues (**Figure 4A**), one of them (W155) located on the surface of the beta sheet and exposed to the solvent, and the other two (W168 and W173) in the core of the protein, both at a Van der Waals distance (~ 4 Å). Tryptophan residues are excellent probes to monitor the FXN unfolding process (**Figure 4B**). Fluorescence spectra corresponding to the native state of these mutants were completely superimposable to that of the wild-type variant, exhibiting a wavelength maximum (λ_{MAX}) of ~335 nm, suggesting as the near-UV CD results that the environment of tryptophan residues is preserved. On the other hand, the urea-induced unfolding resulted in all cases in a λ_{MAX} shift to 350 nm due to the solvent effect over the tryptophan–excited state. This is indicative of a full unfolding process at high urea concentrations (**Figure 4B**).

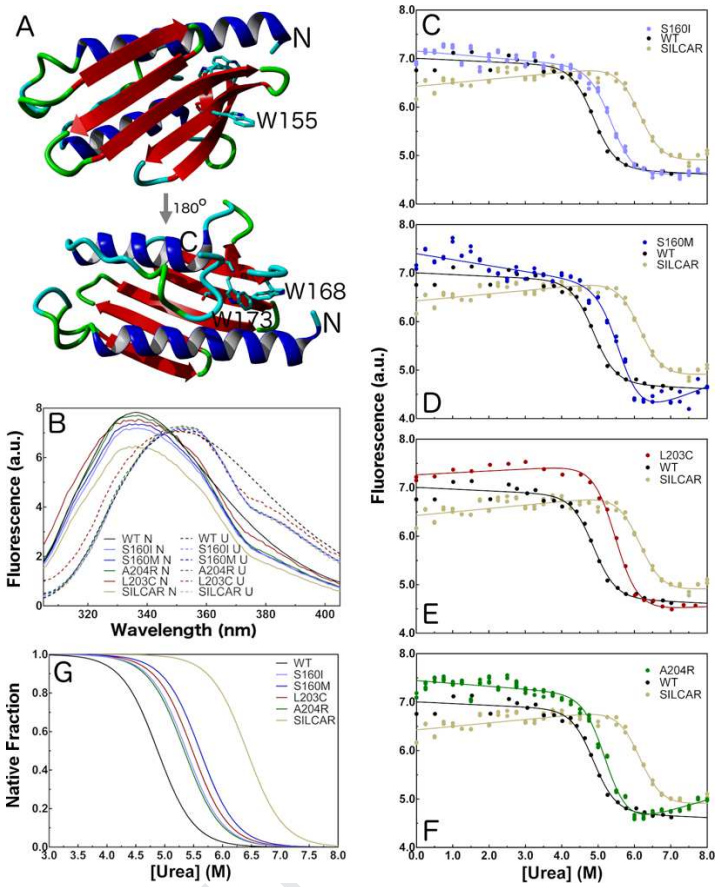

Figure 4. Isothermal Urea-Induced Unfolding Followed by Tryptophan Fluorescence. (A) Tryptophan residues mapped on the human FXN structure (PDB ID 1EKG). (B) Tryptophan spectra corresponding to FXN variants incubated in buffer 20 mM Tris-HCl, 100 mM NaCl, pH 7.0, in the presence of 8 M urea (U, dashed) or in the absence of denaturant (N, solid line). Excitation was performed at 295 nm. Spectra were collected at 20 °C. Protein concentration was 3.7 μM to avoid an inner filter effect. Panels (C), (D), (E) and (F) correspond to S160I, S160M, L203C and A204R, respectively. In panels C-F, the fluorescence intensity at 330 nm was plotted. Wild-type and the triple mutant SILCAR are included in each panel as references. (G) The native fraction calculated from the fitting of a two-state model to the experimental data are shown in panels C-F.

Unfolding profiles showed that all the variants behaved as highly cooperative folding units and the analysis of two-state unfolding model fittings indicated that the conformational stability of S160I, S160M and A204R variants notably increases (**Figure 4** and **Table 2**). The stable variants exhibited higher C_m values (**Table 2**).

To obtain a highly stable variant, we chose to prepare a multiple mutant of FXN. It is worthy of mention that S157I and A193L were avoided because of a reduced

function (see below) and lower observed T_m value, respectively. Therefore, we prepared a triple mutant variant that included S160I, L203C and A204R changes (SILCAR variant). In principle, if the effect of the mutations were completely additive, this variant should be ~3 kcal mol^{-1} more stable than the wild-type (ΔG^{o}_{NU} might reach the 12 kcal mol^{-1}). As expected, the SILCAR variant was structured (**Figure 2**). We evaluated the conformational stability of this variant (ΔG^{o}_{NU}= 11.5 kcal mol^{-1}, **Table 2** and **Figure 4**); taking into account the experimental error of ΔG^{o}_{NU} determinations (~0.25 kcal mol^{-1}), the analysis suggested that the partial effects of the mutations may be approximately additive.

It is worthy of note that the fittings of the two-state model to the data corresponding to the mutants and wild-type FXN were performed with a common m_{NU} parameter (the dependence of unfolding free energy with the chaotropic agent concentration $\frac{\partial \Delta G^{o}_{NU}}{\partial [\mathrm{Urea}]}$) by a global fit of all the data, resulting in a m_{NU} =1.85 ± 0.04 kcal mol^{-1} M^{-1}. The fact that a common m_{NU} could be applied, suggested that the difference in the solvent–accessible surface area (ΔASA_{NU}) between the native and unfolded states may be similar for the variants.

Remarkably, a good correlation between ΔG^{o}_{NU} (at 20°C) and the observed T_m values was obtained (**Figure 5**), reinforcing the idea that the variants share a common ΔS^{o}_{NU} at 20°C (Becktel and Schellman 1987), and suggesting that the variation in ΔG^{o}_{NU} at this temperature is essentially mediated by enthalpic differences among the variants. As previously showed by Schellman (Schellman 1987), this correlation was very useful for screening purposes, in our experiments. Moreover, in the case of the SILCAR variant, the observed T_m value was significantly increased compared to that of the wild-type FXN (ΔT_m ~10 °C, **Table 1**) and the correlation was also very good.

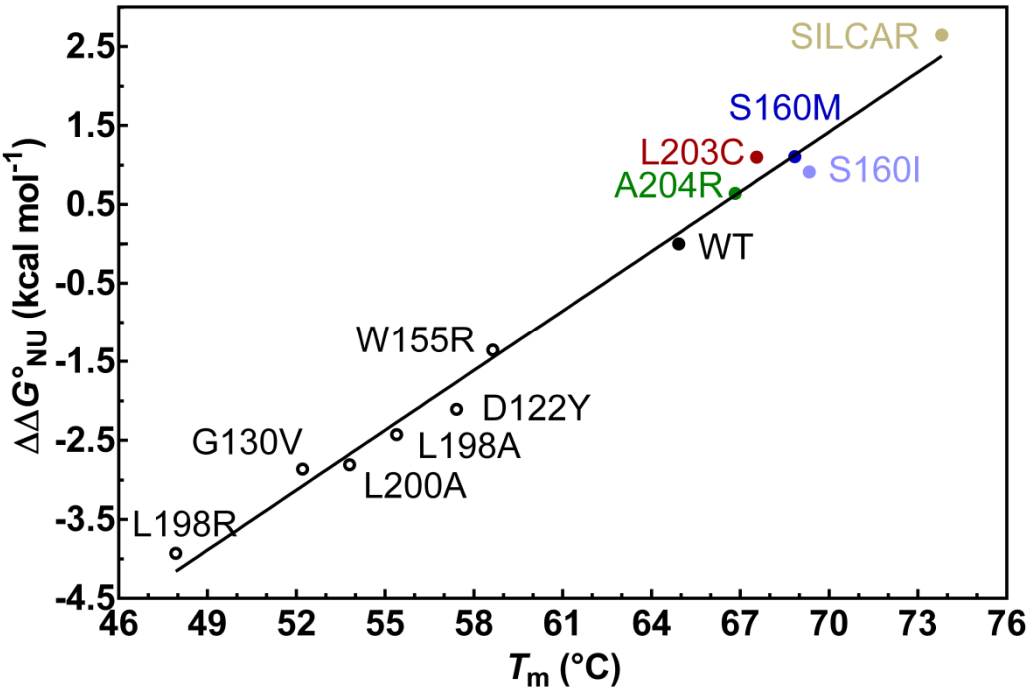

Figure 5. Correlation between the Observed T_m and Conformational Stability. For the correlation we included data corresponding to the variants prepared for this work and the FRDA variants L198R, D122Y, W155R. Also, we included two CTR variants previously studied in our laboratory L198A and L200A. Free energy differences for D122Y, G130V and W155R were taken from (Correia et al. 2008). The black straight line corresponds to the linear correlation (R^2= 0.99). $\Delta\Delta G^{o}_{NU}$ values were calculated as $\Delta\Delta G^{o}_{NU} = \Delta G^{o}_{NU\ \text{mutant FXN}} - \Delta G^{o}_{NU\ \text{wild-type FXN}}$

Resistance to Proteolysis

Resistance to proteolysis comprises a combination of at least two different features of proteins, on the one hand, global stability and, on the other hand, local unfolding events and motions specific for native state dynamics; in both cases proteolytic sites have to be exposed to the protease active site.

At 20-25 °C, wild-type FXN is pretty resistant to proteolysis. When the reaction for wild-type was carried out at room temperature, after long incubation times with chymotrypsin, we observed only a singly cut; it occurred at position Tyr 205, in the C-terminal region. On the other hand, for some FRDA variants like L198R and G130V (Correia et al. 2008), or for the C-terminal truncated FXN 90-195, a distinctive

sensitivity to proteolysis was observed, even with very short incubation times (2 min at 20 ºC) and low protease concentration (1:200, FXN: protease ratio) (Faraj et al. 2014).

Remarkably, at higher temperatures (40 °C), the wild-type variant is considerably more sensitive to chymotrypsin action. In fact, after a five-hour incubation (protein:protease ratio 1:100), FXN was almost completely degraded, only <10 % of the total protein remained intact (elution peak between 34.3-34.6 min, **Figure 6A** and **Table S1**).

In this condition, the stable variants S160I, L203C and A204R showed higher resistance to proteolysis than the wild-type FXN, as judged by the analysis of the RP-HPLC profiles, and the protein persisted intact after protease treatment (elution peak between 34.3-34.6 min, **Figure 6**). Qualitatively, resistance to proteolysis was wild type ~ S160M < L203C < S160I < A204R (**Figures 6A-E**). In particular, the fraction of protein that remained intact in the case of L203C and S160I was approximately 1.7 and 2.7 times (respectively) higher than that what was observed in the case of the wild-type FXN, whereas in the case of mutant A204R, the fraction of intact protein was more than 4.7 times the observed fraction for the wild-type, as judged by the area below the corresponding peaks. Therefore, A204R exhibited considerably higher resistance, compared to the other point mutant. Proteolysis was also evaluated for the SILCAR variant in the same conditions (with 100:1; FXN:chymotrypsin, 40 °C, 5h). SILCAR was significantly more resistant than the wild-type variant (6.3 times, **Table S1**) and the point mutants, and even more resistant than A204R (**Figure 6F**).

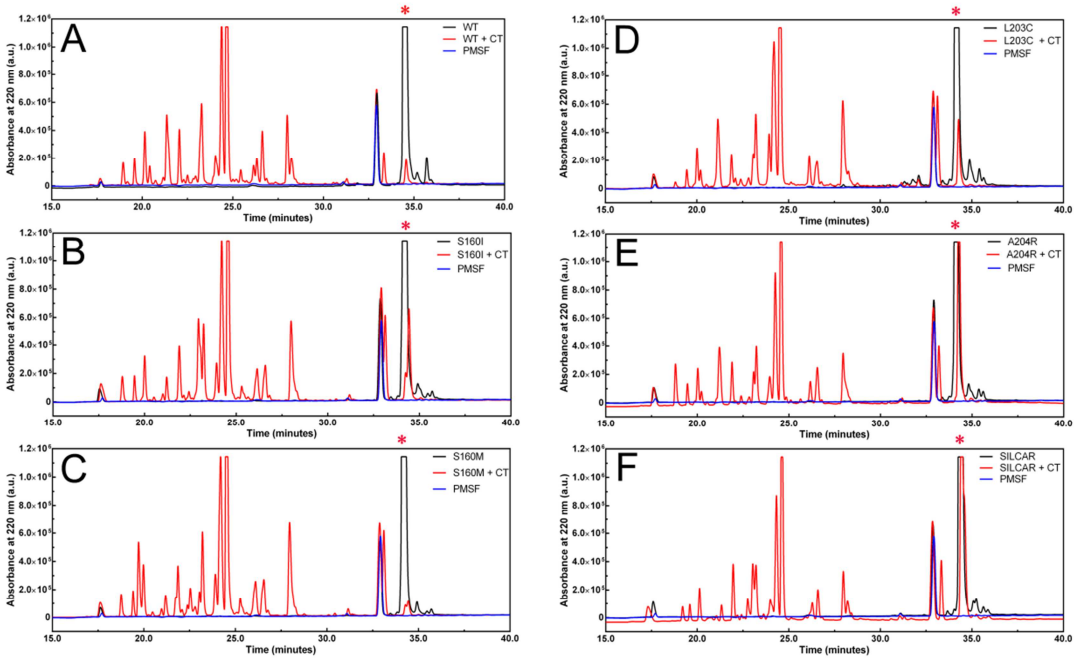

Figure 6. Resistance to Proteolysis of the FXN Variants. RP-HPLC profiles corresponding to wild-type (A), S160I (B), S160M (B), L203C (C), A204R (D) and SILCAR variant (F). In each panel PMSF (blue) and the protein without protease (black) were included. Proteins (1 mg mL^{-1}) were incubated during 5h at 40 °C in buffer 20 mM Tris-HCl, 100mM NaCl, 1mM EDTA, pH 7.0 with 1:100 protease: protein (chymotrypsin). In all cases, the reactions were stopped by the addition of 1mM PMSF (final concentration) and 0.05-0.1% (*v/v*) TFA. After that, a gradient from 0 to 100% acetonitrile (0.05% (*v/v*) TFA) was performed. The column used was analytical C18 (Higgins Analytical, Inc. U.S.A.) and peptides were monitored by absorbance at 220 nm.
The peak corresponding to the intact protein is signaled with a red asterisk at the top of each chromatographic profile. The values corresponding to the integration of the areas are in Table S1.

Activation of Cysteine Desulfurase NFS1 Enzyme and Frataxin Function of the Point Mutants

Does the increase in stability affect the biological function of FXN? To investigate this issue, we evaluated the capability of the FXN mutants to activate the

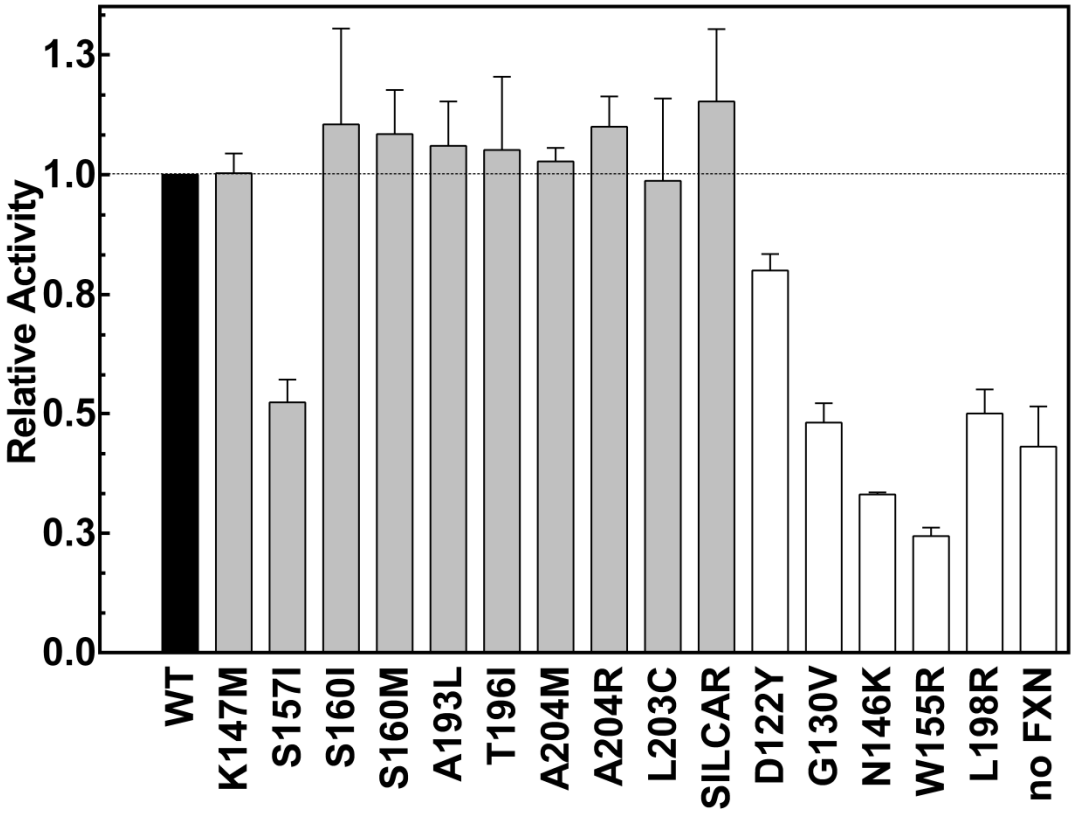

cysteine desulfurase enzyme. With the exception of variant S157I, all the variants showed similar activation to the exhibited by wild-type FXN (**Figure 7**).

Figure 7. Activation of Cysteine Desulfurase NFS1 by the FXN Variants. Enzymatic desulfurization of cysteine to alanine and sulfide by the (NFS1/ACP-ISD11/ISCU/FXN)$_2$ supercomplex was determined by the methylene blue method. Samples were incubated at room temperature for 30 min. H_2S production was stopped and the production of methylene blue was measured by absorbance at 670 nm. Grey bars correspond to the designed variants, whereas white bars correspond to the FRDA FXN variants and a control without FXN (no FXN).

Variant S157I, however, exhibited only 50% of the specific activation of wild-type FXN. It is worthy of note that this variant exhibited only a slightly higher activation than the FRDA mutants N146K and W155R, suggesting a substantial effect of the S157I mutation on function, and possibly, a specific involvement of this residue

in protein-protein interactions, most likely with ISCU, because S157 is located in the β-sheet oriented to the solvent and at only 5Å of the FXN key-residue W155. In fact, the structure of the supercomplex (PDB ID: 6NZU) shows that S157 forms a hydrogen bond with the backbone carbonyl oxygen of residue P133 of the ISCU subunit (**Figure S2**).

Mutant K147M showed an activation similar to that observed for the wild-type FXN, suggesting the possibility of avoiding ubiquitination (which occurs in residue K147) and ubiquitin-mediated degradation *in vivo* (Benini et al. 2017; Rufini et al. 2011), conserving the thermodynamic stability of wild-type protein by compensation of the negative effect of K147M (the observed T_m is approximately 4 °C lower than the observed for the wild-type) by making other mutations.

Whether or not SILCAR was useful to activate cysteine desulfurase NFS1 supercomplex was a major question because it was not clear enough if extreme enhancement stability might result in an increased rigidity or an alteration of other properties that could alter FXN activity. As shown in **Figure 7**, this stable variant was able to activate the supercomplex in the same fashion that wild-type FXN did.

The inspection of a plot of cysteine desulfurase activity *vs.* the observed T_m (**Figure 8**) clearly shows that there is no correlation between stability and function. In fact, it is unlikely that the observed requirement for the activation depends on the native fraction of the FXN given that, even for the most unstable variant assayed in this work (L198R $\Delta G°_{NU}$= 5 kcal M^{-1} (Faraj et al. 2014)), the unfolded fraction is < 0.02 % at room temperature. Furthermore, cysteine desulfurase activation seems to reach a maximal activity to what was observed for the wild-type, independently of the increase in the stability of the variant.

Nevertheless, from a practical point of view, FXN variants can be clustered in four different groups: (i) active and stable variants (relative activity ~1.0 and observed Tm ≥ 65 °C); (ii) active but unstable (relative activity ~1.0 and observed Tm <65 °C); (iii) inactive but stable (relative activity < 1.0 and observed Tm ≥ 65 °C); and (iv) inactive and unstable (relative activity < 1.0 and observed Tm < 65 °C).

The K147M variant exhibits a reduced stability, although this mutant does preserve the protein function (group ii). The FRDA G137V variant recently studied by Faggianelli and coworkers (Faggianelli et al. 2015) is a much more pronounced case of conformational instability in a context of similar activity compared with the wild-type FXN. Variants S157I (prepared in this work) and N146K (FRDA) can be clustered in group iii. On the other hand, the FRDA variants D122Y, G130V, W155R and L198R may be clustered in group iv; they are highly unstable and, simultaneously, they are significantly less active than the wild-type FXN.

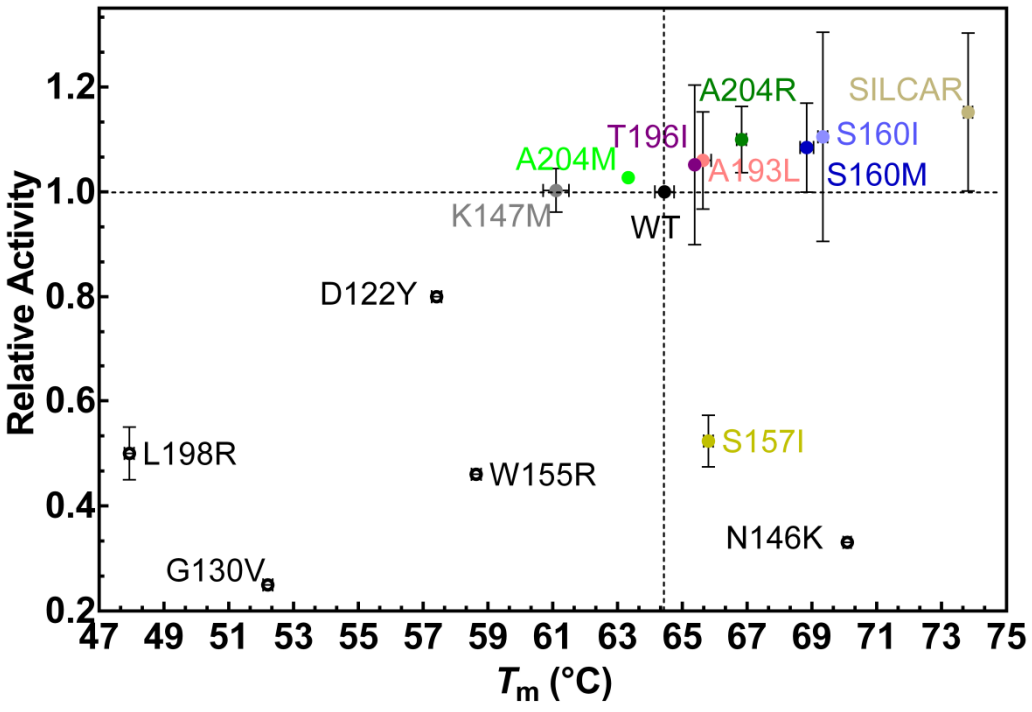

Figure 8. Activation of Cysteine Desulfurase NFS1 by the FXN Variants *vs.* Resistance to Thermal Denaturation. Data shown in Figures 5 and 8 were plotted.

The Conformational Dynamics of the SILCAR Variant

Given that SILCAR variant exhibited remarkable resistance to proteolysis, we wondered whether these three mutations caused an alteration of the internal motions of FXN. To evaluate this issue, first we carried out all-atom molecular dynamics simulations for this mutant and for the wild-type variant (**Figure 9**).

The analysis of the simulations carried out at 27 ºC showed similar RMSF profiles for both variants (**Figure 9A**), suggesting, in principle, comparable internal motions in the nanosecond timescale. A slightly lower internal mobility was observed for wild type, in particular, for stretches 115-121 (that comprises loop 1), 135-140, 158-162 (which includes S160I mutation in SILCAR), and 190-200. When simulations were run at a higher temperature (67 ºC), some stretches of the wild-type variant exhibited higher mobility than SILCAR; nevertheless, other stretches proved to be more dynamic in the case of SILCAR. RMSD analysis showed no significant differences in global mean fluctuations between the wild-type and SILCAR nor in the C-terminal average motions (data not shown).

Interestingly, the interactions that R204 can establish seem to depend on the temperature. When simulations were carried out at 27 ºC, the side chain of R204 established strong ionic interactions with E101 and also interacted with other acidic residues (D104 and E108) in SILCAR (**Figure 9B**). On the other hand, when simulations were run at 67 ºC the strongest interaction was formed between R204 and D104, whereas E101 and E108 only sporadically formed ionic pairs with the arginine, as judged by the distance analysis (**Figure 9B**). Additionally, Y205 established a stronger hydrogen bond interaction with E101 in the case of the SILCAR variant

compared to the wild-type FXN, and this was also evident when simulations were run at a higher temperature (**Figure 9C**).

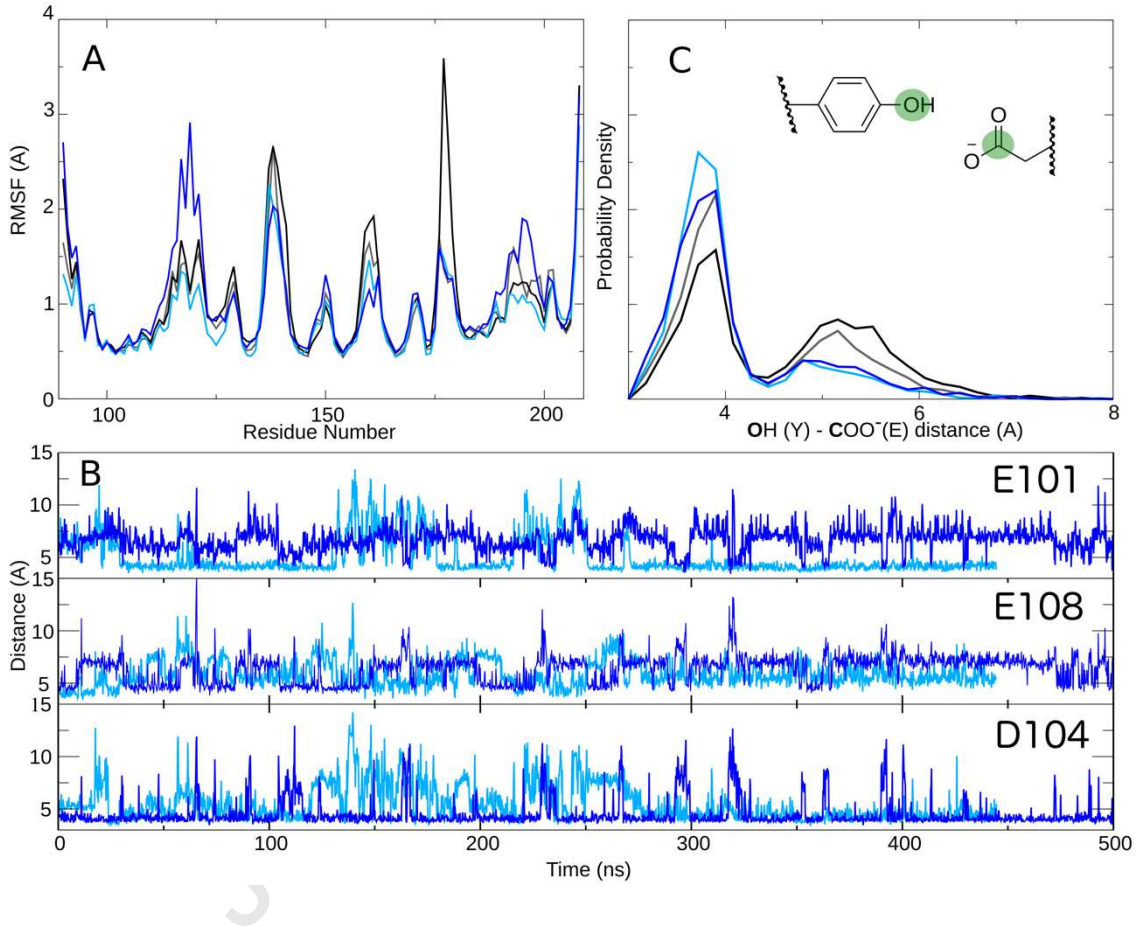

Figure 9. Internal Motions of Human FXN Explored by Molecular Dynamics Simulations. (A) RMSF values corresponding to the wild-type (gray and black at 27 ºC and 67 ºC, respectively) and SILCAR (cyan and blue at 27 ºC and 67 ºC, respectively) variants. (B) Interaction distance between R204 and E101, D104 or E108 along the simulation time of SILCAR. (C) Histogram showing the distribution of the observed distances between residues Y205 and E101 along the simulation time of the wild-type (gray and black at 27 and 67 ºC, respectively) and SILCAR (cyan and blue at 27 and 67 ºC, respectively) variants.

We calculated the fraction of time in which the H-bond between Y205 and E101 was formed. For the wild-type protein, 60% was estimated when simulated at 27 ºC and 50% when the temperature was increased to 67 ºC. In the SILCAR variant simulations,

this interaction was present 80% and 75% of the time at 27 and 67 ºC, respectively. This behavior may be related to the high resistance of SILCAR to chymotrypsin; that is, Y205 would be more rigid and structured in the case of SILCAR and consequently, less accessible to protease action.

Internal motions spread in a broad range of timescales. We wondered whether SILCAR exhibited alterations in its dynamics, in the range of the microsecond to milliseconds that might be relevant in protein function. Carr-Purcell-Meiboom-Gill (CPMG) relaxation dispersion NMR experiments are useful to explore motions in this timescale; thus we carried out this experiment for the ^{15}N-labeled SILCAR and wild-type FXN variants, for comparison (**Figure 10**).

Prior to that, in the case of the SILCAR variant, the assignments were corroborated by means of NOESY-HSQC and TOCSY-HSQC spectra, because an important set of H-^{15}N- groups exhibited significant chemical shift differences (**Figure 10A**) compared to that of the wild-type FXN. Higher differences were observed for residues close in space to the mutation sites (S160I, L203C and A204R, **Figures S3 and S4**).

If some residues were involved in a conformational exchange that occurs in this timescale, this exchange should positively contribute to the observed (effective) transversal relaxation (R_2^{obs}). Additionally, an increase in k_{ex} (the observed kinetic constant for the exchange process), or an increment in the population of the excited state (higher in energy than the ground state), or an increase in the difference between the chemical shifts of the excited state and the ground state may result in an increase in the observed transversal relaxation rates (R_2^{obs}) (Mittermaier and Kay 2006; Mittermaier and Kay 2009; Palmer et al. 2001).

The results indicate that the relaxation profiles corresponding to the variants are similar. Thus, in principle, both the SILCAR and the wild-type variants exhibit similar internal motions. However, some residues exhibiting high R_2^{obs} values in the wild-type variant have shown even higher values in SILCAR, suggesting that the exchange might be higher in the mutant (**Figures 10B and C**). To study what the source of these differences was, we carried out two-state (ground and excited native states) global fittings (**Figures 10D and E**) using the Sherekhan server (Mazur et al. 2013), considering data sets acquired at two different magnetic field strengths (14.1 and 16.5 T). The analysis of the global fittings suggests that there are no significant differences in the conformational exchange rate (k_{ex} are 225 ± 31 and 216 ± 16 s^{-1} for wild-type and SILCAR, respectively) nor are there any changes in the populations of ground and excited states (p_B are 0.016 ± 0.002 and 0.019 ± 0.002, for wild-type and SILCAR variants, respectively). Therefore, the origin of the increase in the effective R_2^{obs} values for these residues might come from a slight change in differences in the chemical shifts between the ground and excited states (Δω, **Figure 10D**). Thus, these peculiarities observed for the R_2^{obs} values in SILCAR are more likely evidence of the subtle effects of the three mutations on the fine structure of the ground and/or excited states rather than alterations in the dynamics of the protein.

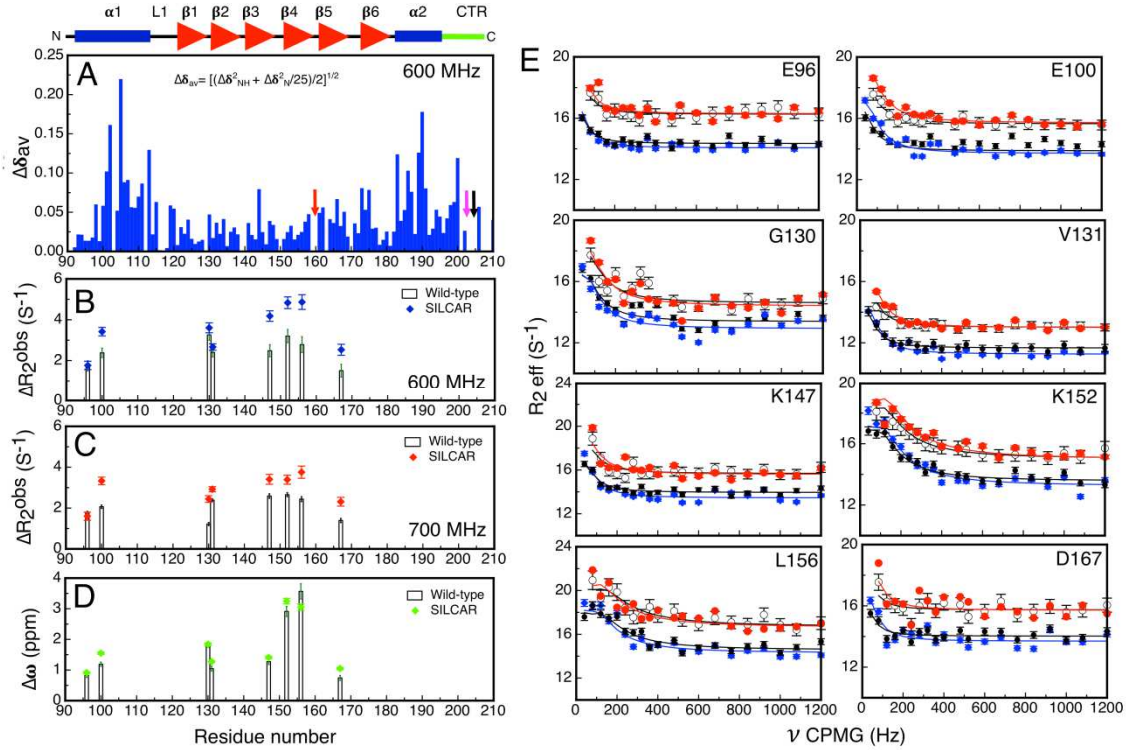

Figure. 10. NMR analysis of the SILCAR variant. (A) Chemical Shift Perturbation (CSP). ^{1}H-^{15}N HSQC spectra corresponding to wild-type and SILCAR variants were analyzed to identify the effect of point mutations on the amide chemical shift using the parameter $\Delta\delta = [(\Delta\delta^2_H + \Delta\delta^2 N/25)/2]^{0.5}$. The small arrows indicate the mutated residues in SILCAR, 160, 203 and 204. (B) The contribution of a conformational exchange to transverse relaxation, ΔR_2^{obs}, was estimated from the difference in R_2^{obs} at the lowest and highest CPMG frequency values and plotted along the FXN sequence (diamonds in blue and black bars correspond to the SILCAR and wild-type variants, respectively). The experiment was carried out at 14.1 T. (C) Similar to panel B, but the experiment was performed at 16.5 T. For clarity, only the subset of residues used for global fittings (E96, E100, G130, V131, K147, K152, L156 and D167) is shown. (D) The differences in chemical shifts between the ground and excited states from fittings to the Carver-Richards equation (see the Materials and Methods section) for the same subset of residues as in panel B. (E) The global fittings using data acquired at 14.1 (black-bold and blue circles, wild-type and SILCAR, respectively) and 16.5 T (black-empty and red-bold circles , wild-type and SILCAR, respectively). The residue corresponding to the cross-peak analyzed is indicated in each panel. Lines indicate the best-fit curves obtained using shared values for the exchange rate and state populations, according to previous work (Noguera et al. 2017). The residues analyzed are plotted on the FXN structure in **Figure S5**, in Supplementary Material).

Discussion

FXN Variants with High Conformational Stability

In this study we explored the structure of FXN in order to find mutants with higher stability than the wild-type protein and similar biological activity. We identified several candidates by means of the FOLDX computational tool. Seven mutants were prepared and studied. Three of them (S160I, S160M and A204R) were significantly more stable than the wild-type variant and equally active as cysteine desulfurase NFS1 activators. Thus, these variants and L203C, previously studied in our laboratory, provided a good tool to explore structural dynamics-activity relationships spanning a broad range of conformational stabilities.

Taking into account the structure of FXN (PDB ID 1EKG), the structure of the supercomplex for the iron-sulfur cluster assembly (PDB ID 6NZU) and the computational models corresponding to the point mutant FXN variants, the following inferences can be made regarding the effect of the mutations on stability and function:

K147M: Residue K147 establishes an ionic interaction with E96 (2.5Å). It might be inferred that this mutation can reduce the stability of the protein, cancelling this salt bridge. On the other hand, methionine might establish apolar interactions with L103 side chain (3.1 Å). The experimental results indicate that a destabilizing effect of the mutation prevailed.

S157I: This variant exhibits a slightly higher observed T_m value than the wild-type variant. I157 might establish stabilizing apolar contacts with V144 (distance is 3.7 Å). On the other hand, it is not odd that the S157I variant is a very poor activator of the cysteine desulfurase NFS1 supercomplex because S157 appears to form a hydrogen bond with P133 from ISCU (**Figure S2**) and the mutation cancels this interaction.

S160I: As predicted by FOLDX, it is more stable than the wild-type FXN. The analysis of the FXN structure suggests that the isoleucine at position 160 might

establish apolar interaction with P159 (3.5 Å), stabilizing the β-turn structure between the β-strands 4 and 5.

S160M: It is more stable than the wild-type variant. A methionine residue in that place may interact with P159 and also with E189 (3.6 and 3.5 Å, respectively).

A193L: It is more stable than the wild-type; it is likely that leucine increases the number of apolar contacts with residues at the core of FXN: L140, L136 and Y143 (3.4, 3.6 and 3.3 Å, respectively).

T196I: The analysis of the structure suggests that isoleucine located in the first part of CTR region might interact with Tyr 108 from loop 1, making an apolar bridge. However, the fact that the observed T_m values corresponding to wild-type and T196I are very similar suggests that, if this interaction takes place, it is only transient or, on the other hand, the effect is negatively compensated in some way.

L203C: As previously described (Faraj et al. 2016; Faraj et al. 2019), a cysteine residue at position 203 can favorably interact with apolar side chains of the FXN core, whereas it can also interact with core polar residues such as H183 and S105 (distances= 3.4 and 3.3 Å, respectively) given its dual physicochemical behavior, which is not properly predicted by FOLDX or Dynamut software.

A204M: It exhibits a slight destabilizing effect compared to the wild-type variant, as judged by the observed T_m. It is possible that the larger apolar side-chain cannot be properly accommodated at this site.

A204R: it exhibits a marked gain in stability; the analysis of the structure indicates that R204 can establish a strong ionic interaction with E101.

In this work, we also carried out controlled proteolysis of the mutant proteins. Variants S160I, L203C and A204R showed more resistance than the wild-type FXN. In particular, A204R variant showed the highest resistance among the simple mutants.

This arginine residue might create a new salt bridge between the CTR and helix α1. In this regard, relationships between conformational stability and C-terminal region (CTR) integrity of the FXN protein family were previously identified (Roman et al. 2012; Adinolfi et al. 2004). Furthermore, it was shown that CTR mutations essentially affect the stability of the native state but neither the stability of the folding transition state nor that of the intermediary state of the folding reaction (Faraj et al. 2016) are altered.

Moreover, point mutation L198R at the CTR locally alters FXN internal motions. This behavior was also studied in detail in our laboratory by means of the engineered cysteine point mutants (located in the core: V134C, located in the CTR: L198C, L200C and L203C) and thiol-disulfide exchange dynamics. These experiments effectively showed that there is a correlation between local stability of the CTR and global stability of FXN (Faraj et al. 2019). On the other hand, complete truncation of the CTR (Δ195) perturbed internal motions in a global fashion, suggesting a conformational exchange between the native and unfolded states in the absence of a denaturant and at room temperature (Faraj et al. 2014). This is in agreement with the very low conformational stability of the CTR truncated variant (Roman et al. 2012).

To increase the stability of FXN, we have prepared the triple mutant SILCAR (S160I/L203C/A204R). Remarkably, SILCAR has two-point mutations located in the CTR. As expected, this variant was highly stable. Moreover, SILCAR was as active as the wild-type FXN and, notably, it was more resistant to proteolysis than each one of the simple mutants, suggesting a more compact structure.

Relaxation dispersion NMR experiments have shown that this mutant has internal motions similar to that of the wild-type variant at least in the micro-millisecond timescale. In this context, the fact that SILCAR was more resistant to chymotrypsin

protease suggests the protection at specific proteolytic sites, a hypothesis that will be further investigated.

The capability of human FXN to exert its function *in vivo* seems to depend on a multiplicity of factors, among them: expression levels, ubiquitination and degradation (Rufini et al. 2015; Rufini et al. 2011), translocation and processing of the precursor (1-210) and intermediate (41-210) forms to yield the mature form (81-210) within the mitochondrial matrix, conformational stability, the establishment of proper protein-protein interactions (cysteine desulfurase NFS1 supercomplex), iron interaction and perhaps the inhibition of protein aggregation, which was described for some pathogenic variants in vitro (Correia et al. 2014; Correia et al. 2008). All these features make the essence of FXN inside the cell.

Whether a highly stable variant as SILCAR is able to act as the wild-type FXN should be explored in more detail. Here we explored only a small part of the picture. More experiments should be done to evaluate if SILCAR is able to activate the [Fe-S] cluster assembly and if other possible moonlight functions of FXN inside the cells are carried out in a proper way by this variant. In this context, the combination of SILCAR mutations with K147M or K147R—which are less stable than the wild-type FXN but would not be substrates of the ubiquitin-mediated protein degradation pathway—may be good options to prepare a highly stable *in vivo* FXN variant for protein replacement therapies.

Table 1. Parameters for FXN Variants

Variant	Properties and Predictions					
	Theoretical Molecular Mass [a] (Da)	Experimental Molecular Mass (Da)	R_H [b] (nm)	FOLDX Stability [c, d] (kcal mol^{-1})	Dynamut Stability [e] (kcal mol^{-1})	Temperature-Induced Unfolding [f] Observed T_m (°C)
Wild type	13605.2	13604.9±0.3	2.0±0.3	---	---	64.9 ± 0.6
K147M	13608.2	13607.7	1.9±0.1	2.1	0.2	61.1± 0.4
S157I	13631.2	13630.4	2.5±0.1	2.7	1.7	65.8 ± 0.2
S160I	13631.2	13630.0	2.4±0.2	0.9	1.1	69.3 ± 0.2
S160M	13649.3	13647.3	2.3±0.2	2.3	1.5	68.8 ± 0.2
A193L	13647.2	13646.0	2.1±0.1	2.2	2.0	65.7 ± 0.3
T196I	13617.2	13617.2	2.4±0.1	0.9	0.1	65.4 ± 0.2
L203C	13595.1	13600.0 [h]	2.0±0.2	-2.9	-1.0	67.6 ± 0.2
A204M	13665.3	13664.0	2.0±0.2	0.3	0.2	63.3 ± 0.1
A204R	13690.3	13689.2	1.8±0.3	0.5	-0.3	66.8 ± 0.2
SILCAR[g]	13706.3	13705.5	2.5±0.1	---	---	73.8 ± 0.1

[a] Theoretical parameter inferred from the protein sequences calculated using EXPASY tool (Wilkins et al. 1999).
[b] It was evaluated by DLS. Protein concentration was in the range 1-2 mg mL^{-1}. Size distributions were weighted by particle number.
[c] $\Delta\Delta G°_{NU}$ calculated using PDB ID: 1EKG (Dhe-Paganon et al. 2000).
[d] Calculated using FOLDX repair tool (Schymkowitz et al. 2005). Negative and positive values indicate destabilization and stabilization, respectively. Prior to stability calculation repair algorithm was applied. The analysis of the different FOLDX terms that contribute to the stability of each variant is shown in Figure S1.
[e] Negative and positive Dynamut (Rodrigues et al. 2018) values indicate destabilization and stabilization, respectively (a correlation between FOLDX and Dynamut results is shown in Figure S1).
[f] Observed T_m was derived from temperature-induced unfolding experiments followed by Sypro-orange fluorescence.
[g] The triple mutant variant S160I/L203C/A204R.
[h] Mass measured by MALDI TOF. The rest of the variants were analyzed by ESI-MS as mentioned in Materials and Methods.

Table 2. Thermodynamic Parameters for Equilibrium Unfolding of FXN Variants

Variant	Urea-Induced Unfolding [a]		
	C_m (M)	$\Delta G°_{NU, H20}$ (kcal mol^{-1})	$\Delta\Delta G°_{NU}$ (kcal mol^{-1})
Wild type	4.88	9.02 ± 0.16	-----
S160I	5.37	9.94 ± 0.08	0.92
S160M	5.34	9.88 ± 0.25	0.86
L203C	5.48	10.14 ± 0.08	1.12
A204R	5.23	9.67 ± 0.07	0.65
SILCAR	6.20	11.46± 0.06	2.44 (2.69) [b]

[a] Parameters were obtained by least-squares fitting using a globally adjusted value of m_{NU} = 1.85 ± 0.04 kcal mol^{-1} M^{-1} (Faraj et al. 2016).

[b] The value between parenthesis was calculated as: $\Delta\Delta G°_{NU\ SILCAR} = \Delta\Delta G°_{NU\ S160I} + \Delta\Delta G°_{NU\ L203C} + \Delta\Delta G°_{NU\ A204R}$

Acknowledgments

We thank Dr. María Laura Cerutti (CRIP, UNSAM) for her support concerning the R_h determination of proteins by DLS. JS thanks CONICET and Universidad de Buenos Aires for financial support.

Funding Sources

This study was supported by the *Agencia Nacional de Promoción Científica y Tecnológica* (ANPCyT) through grant No. PICT 2016-2280, the *Consejo Nacional de Investigaciones Científicas y Técnicas* (CONICET), and the Friedreich's Ataxia Research Alliance (FARA).

UniProt Accession IDs

Q9HD34: human LYR motif-containing protein 4 (ISD11); O14561: human mitochondrial acyl carrier protein (ACP); Q9Y697: human cysteine desulfurase (NFS1); Q9H1K1: human Iron-sulfur cluster assembly enzyme (ISCU); Q16595: human frataxin (FXN).

References

Adinolfi S, Nair M, Politou A, Bayer E, Martin S, Temussi P, Pastore A (2004) The factors governing the thermal stability of frataxin orthologues: how to increase a protein's stability. Biochemistry 43 (21):6511-6518

Adinolfi S, Trifuoggi M, Politou AS, Martin S, Pastore A (2002) A structural approach to understanding the iron-binding properties of phylogenetically different frataxins. Hum Mol Genet 11 (16):1865-1877

Becktel WJ, Schellman JA (1987) Protein stability curves. Biopolymers 26 (11):1859-1877

Bellanda M, Maso L, Doni D, Bortolus M, De Rosa E, Lunardi F, Alfonsi A, Noguera ME, Herrera MG, Santos J, Carbonera D, Costantini P (2019) Exploring iron-binding to human frataxin and to selected Friedreich ataxia mutants by means of NMR and EPR spectroscopies. Biochim Biophys Acta Proteins Proteom 1867 (11):140254

Benini M, Fortuni S, Condo I, Alfedi G, Malisan F, Toschi N, Serio D, Massaro DS, Arcuri G, Testi R, Rufini A (2017) E3 Ligase RNF126 Directly Ubiquitinates Frataxin, Promoting Its Degradation: Identification of a Potential Therapeutic Target for Friedreich Ataxia. Cell Rep 18 (8):2007-2017

Bieri M, Gooley PR (2011) Automated NMR relaxation dispersion data analysis using NESSY. BMC Bioinformatics 12:421

Bridwell-Rabb J, Winn AM, Barondeau DP (2011) Structure-function analysis of Friedreich's ataxia mutants reveals determinants of frataxin binding and activation of the Fe-S assembly complex. Biochemistry 50 (33):7265-7274

Campuzano V, Montermini L, Molto MD, Pianese L, Cossee M, Cavalcanti F, Monros E, Rodius F, Duclos F, Monticelli A, Zara F, Canizares J, Koutnikova H, Bidichandani SI, Gellera C, Brice A, Trouillas P, De Michele G, Filla A, De Frutos R, Palau F, Patel PI, Di Donato S, Mandel JL, Cocozza S, Koenig M, Pandolfo M (1996) Friedreich's ataxia: autosomal recessive disease caused by an intronic GAA triplet repeat expansion. Science 271 (5254):1423-1427

Candayan A, Yunisova G, Cakar A, Durmus H, Basak AN, Parman Y, Battaloglu E (2019) The first biallelic missense mutation in the FXN gene in a consanguineous Turkish family with Charcot-Marie-Tooth-like phenotype. Neurogenetics

Capece L, Marti MA, Crespo A, Doctorovich F, Estrin DA (2006) Heme protein oxygen affinity regulation exerted by proximal effects. J Am Chem Soc 128 (38):12455-12461

Case DA, Ben-Shalom IY, Brozell SR, Cerutti DS, Cheatham TE, Cruzeiro VWD, Darden TA, Duke RE, Ghoreishi D, Gilson MK, Gohlke H, Goetz AW, Greene D, Harris R, Homeyer N, Izadi S, Kovalenko A, Kurtzman T, Lee TS, LeGrand S, Li P, Lin C, Liu J, Luchko T, Luo R, Mermelstein DJ, Merz KM, Miao Y, Monard G, Nguyen C, Nguyen H, Omelyan I, Onufriev A, Pan F, Qi R, Roe DR, Roitberg A, Sagui C, Schott-Verdugo S, Shen J, Simmerling CL, Smith J, Salomon-Ferrer R, Swails J, Walker RC, Wang J, Wei H, Wolf RM, Wu X, Xiao L, York DM, Kollman PA (2018) AMBER 2018. University of California, San Francisco

Correia AR, Naik S, Fisher MT, Gomes CM (2014) Probing the kinetic stabilities of Friedreich's ataxia clinical variants using a solid phase GroEL chaperonin capture platform. Biomolecules 4 (4):956-979

Correia AR, Pastore C, Adinolfi S, Pastore A, Gomes CM (2008) Dynamics, stability and iron-binding activity of frataxin clinical mutants. FEBS J 275 (14):3680-3690

Correia AR, Wang T, Craig EA, Gomes CM (2010) Iron-binding activity in yeast frataxin entails a trade off with stability in the alpha1/beta1 acidic ridge region. Biochem J 426 (2):197-203

Delaglio F, Grzesiek S, Vuister GW, Zhu G, Pfeifer J, Bax A (1995) NMRPipe: a multidimensional spectral processing system based on UNIX pipes. J Biomol NMR 6 (3):277-293

Dhe-Paganon S, Shigeta R, Chi YI, Ristow M, Shoelson SE (2000) Crystal structure of human frataxin. J Biol Chem 275 (40):30753-30756

Faggianelli N, Puglisi R, Veneziano L, Romano S, Frontali M, Vannocci T, Fortuni S, Testi R, Pastore A (2015) Analyzing the Effects of a G137V Mutation in the FXN Gene. Front Mol Neurosci 8:66

Faraj SE, Gonzalez-Lebrero RM, Roman EA, Santos J (2016) Human Frataxin Folds Via an Intermediate State. Role of the C-Terminal Region. Sci Rep 6:20782

Faraj SE, Noguera ME, Delfino JM, Santos J (2019) Global Implications of Local Unfolding Phenomena, Probed by Cysteine Reactivity in Human Frataxin. Sci Rep 9 (1):1731

Faraj SE, Roman EA, Aran M, Gallo M, Santos J (2014) The alteration of the C-terminal region of human frataxin distorts its structural dynamics and function. FEBS J 281 (15):3397-3419

Farber PJ, Mittermaier A (2015) Relaxation dispersion NMR spectroscopy for the study of protein allostery. Biophysical Reviews 7 (2):191-200

Fox NG, Yu X, Feng X, Bailey HJ, Martelli A, Nabhan JF, Strain-Damerell C, Bulawa C, Yue WW, Han S (2019) Structure of the human frataxin-bound iron-sulfur cluster assembly complex provides insight into its activation mechanism. Nat Commun 10 (1):2210

Galea CA, Huq A, Lockhart PJ, Tai G, Corben LA, Yiu EM, Gurrin LC, Lynch DR, Gelbard S, Durr A, Pousset F, Parkinson M, Labrum R, Giunti P, Perlman SL, Delatycki MB, Evans-Galea MV (2016) Compound heterozygous FXN mutations and clinical outcome in friedreich ataxia. Annals of Neurology 79 (3):485-495

Huang J, Dizin E, Cowan JA (2008) Mapping iron binding sites on human frataxin: implications for cluster assembly on the ISU Fe-S cluster scaffold protein. J Biol Inorg Chem 13 (5):825-836

Johnson BA (2004) Using NMRView to visualize and analyze the NMR spectra of macromolecules. Methods Mol Biol 278:313-352

Jorgensen WL, Chandrasekhar J, Madura JD (2015) Comparison of simple potential functions for simulating liquid water. J Chem Phys 79:926-935

Krieger E, Vriend G (2014) YASARA View - molecular graphics for all devices - from smartphones to workstations. Bioinformatics 30 (20):2981-2982

Lamont PJ, Davis MB, Wood NW (1997) Identification and sizing of the GAA trinucleotide repeat expansion of Friedreich's ataxia in 56 patients. Clinical and genetic correlates. Brain 120 (Pt 4):673-680

Li Y, Lu Y, Polak U, Lin K, Shen J, Farmer J, Seyer L, Bhalla AD, Rozwadowska N, Lynch DR, Butler JS, Napierala M (2015) Expanded GAA repeats impede transcription elongation through the FXN gene and induce transcriptional silencing that is restricted to the FXN locus. Hum Mol Genet 24 (24):6932-6943

Lufino MM, Silva AM, Nemeth AH, Alegre-Abarrategui J, Russell AJ, Wade-Martins R (2013) A GAA repeat expansion reporter model of Friedreich's ataxia recapitulates the genomic context and allows rapid screening of therapeutic compounds. Hum Mol Genet 22 (25):5173-5187

Maier JA, Martinez C, Kasavajhala K, Wickstrom L, Hauser KE, Simmerling C (2015) ff14SB: Improving the Accuracy of Protein Side Chain and Backbone Parameters from ff99SB. J Chem Theory Comput 11 (8):3696-3713

Marmolino D, Acquaviva F (2009) Friedreich's Ataxia: from the (GAA)n repeat mediated silencing to new promising molecules for therapy. Cerebellum 8 (3):245-259

Mazur A, Hammesfahr B, Griesinger C, Lee D, Kollmar M (2013) ShereKhan--calculating exchange parameters in relaxation dispersion data from CPMG experiments. Bioinformatics 29 (14):1819-1820

Mittermaier A, Kay LE (2006) New tools provide new insights in NMR studies of protein dynamics. Science 312 (5771):224-228

Mittermaier AK, Kay LE (2009) Observing biological dynamics at atomic resolution using NMR. Trends Biochem Sci 34 (12):601-611

Musco G, de Tommasi T, Stier G, Kolmerer B, Bottomley M, Adinolfi S, Muskett FW, Gibson TJ, Frenkiel TA, Pastore A (1999) Assignment of the 1H, 15N, and 13C resonances of the C-terminal domain of frataxin, the protein responsible for Friedreich ataxia. J Biomol NMR 15 (1):87-88

Noguera ME, Aran M, Smal C, Vazquez DS, Herrera MG, Roman EA, Alaimo N, Gallo M, Santos J (2017) Insights on the conformational dynamics of human frataxin through modifications of loop-1. Arch Biochem Biophys 636:123-137

Ohshima K, Montermini L, Wells RD, Pandolfo M (1998) Inhibitory effects of expanded GAA.TTC triplet repeats from intron I of the Friedreich ataxia gene on transcription and replication in vivo. J Biol Chem 273 (23):14588-14595

Palmer AG, 3rd, Kroenke CD, Loria JP (2001) Nuclear magnetic resonance methods for quantifying microsecond-to-millisecond motions in biological macromolecules. Methods Enzymol 339:204-238

Punga T, Buhler M (2010) Long intronic GAA repeats causing Friedreich ataxia impede transcription elongation. EMBO Mol Med 2 (4):120-129

Rodrigues CH, Pires DE, Ascher DB (2018) DynaMut: predicting the impact of mutations on protein conformation, flexibility and stability. Nucleic Acids Res 46 (W1):W350-W355

Roman EA, Faraj SE, Gallo M, Salvay AG, Ferreiro DU, Santos J (2012) Protein stability and dynamics modulation: the case of human frataxin. PLoS One 7 (9):e45743

Rufini A, Cavallo F, Condo I, Fortuni S, De Martino G, Incani O, Di Venere A, Benini M, Massaro DS, Arcuri G, Serio D, Malisan F, Testi R (2015) Highly specific ubiquitin-competing molecules effectively promote frataxin accumulation and partially rescue the aconitase defect in Friedreich ataxia cells. Neurobiol Dis 75:91-99

Rufini A, Fortuni S, Arcuri G, Condo I, Serio D, Incani O, Malisan F, Ventura N, Testi R (2011) Preventing the ubiquitin-proteasome-dependent degradation of frataxin, the protein defective in Friedreich's ataxia. Hum Mol Genet 20 (7):1253-1261

Ryckaert J-P, Ciccotti G, Berendsen HJC (1977) Numerical integration of the cartesian equations of motion of a system with constraints: molecular dynamics of n-alkanes. Journal of Computational Physics 23 (3):327-341

Sacca F, Marsili A, Puorro G, Antenora A, Pane C, Tessa A, Scoppettuolo P, Nesti C, Brescia Morra V, De Michele G, Santorelli FM, Filla A (2013) Clinical use of frataxin measurement in a patient with a novel deletion in the FXN gene. J Neurol 260 (4):1116-1121

Schellman JA (1987) The thermodynamic stability of proteins. Annu Rev Biophys Biophys Chem 16:115-137

Schmucker S, Martelli A, Colin F, Page A, Wattenhofer-Donze M, Reutenauer L, Puccio H (2011) Mammalian frataxin: an essential function for cellular viability through an interaction with a preformed ISCU/NFS1/ISD11 iron-sulfur assembly complex. PLoS One 6 (1):e16199

Schymkowitz J, Borg J, Stricher F, Nys R, Rousseau F, Serrano L (2005) The FoldX web server: an online force field. Nucleic Acids Res 33 (Web Server issue):W382-388

Silva AM, Brown JM, Buckle VJ, Wade-Martins R, Lufino MM (2015) Expanded GAA repeats impair FXN gene expression and reposition the FXN locus to the nuclear lamina in single cells. Hum Mol Genet 24 (12):3457-3471

Tsai CL, Barondeau DP (2010) Human frataxin is an allosteric switch that activates the Fe-S cluster biosynthetic complex. Biochemistry 49 (43):9132-9139

Vazquez DS, Agudelo WA, Yone A, Vizioli N, Aran M, Gonzalez Flecha FL, Gonzalez Lebrero MC, Santos J (2015) A helix-coil transition induced by the metal ion interaction with a grafted iron-binding site of the CyaY protein family. Dalton Trans 44 (5):2370-2379

Wilkins MR, Gasteiger E, Bairoch A, Sanchez JC, Williams KL, Appel RD, Hochstrasser DF (1999) Protein identification and analysis tools in the ExPASy server. Methods Mol Biol 112:531-552